Supplementary Information for

Solvent Co-assembly in Lead-free Perovskite Scintillators for Stable and Large-area X-ray Imaging

Lulu Liu[1], Weijun Li[1], Wanting Pan[1], Haotong Wei[1,2*], and Bai Yang[1,2]

[1]*State Key Laboratory of Supramolecular Structure and Materials, College of Chemistry, Jilin University, Changchun, 130012, P. R. China*

[2]*Optical Functional Theranostics Joint Laboratory of Medicine and Chemistry, The First Hospital of Jilin University, Changchun, 130012 P. R. China*

[*]Correspondence to H.W. at Email: hweichem@jlu.edu.cn.

Scintillator light yield (*LY*) test：

According to the definition of *LY*: the number of photons emitted by the scintillator to absorb per unit of X-ray energy. The *LY* of $(DABA)_2MnBr_4 \cdot H_2O$ was derived according to the following equations:

$$LY = \frac{n_{ph}}{E} \tag{S1}$$

$$n_{ph} = \frac{I_0}{hv} \tag{S2}$$

$$E = D/\mu_m \tag{S3}$$

where n_{ph} is the number of photons emitted by the scintillator, E is X-ray energy, I_0 is the emission light intensity, hv is the emission photon energy, D is X-ray dose rate, μ_m is mass attenuation coefficient.

To quantify the X-ray scintillation property, we placed the $(DABA)_2MnBr_4 \cdot H_2O$ wafer on the Si photodiode detector. When the X-ray dose rate is applied, the X-ray will penetrate the scintillator and generate excitons inside. Then the $(DABA)_2MnBr_4 \cdot H_2O$ scintillator emits green fluorescence and is collected by the Si photodiode detector. We measured the response signal with and w/o a thin black paper placed between scintillator with Si photodiode detector under various dose rates. The photocurrent of the $(DABA)_2MnBr_4 \cdot H_2O$ scintillator at different X-ray dose rates is converted into the corresponding light intensity. In detail, according to the following equations:

$$R = \frac{q \times EQE_{si}}{hv} \tag{S4}$$

$$I_0 = \frac{I_S}{R \times S} \quad \text{(S5)}$$

where R is the responsivity, q is the quantity of electric charge. EQE_{Si} is the quantum efficiency of the Si photodiode detector, h is the Planck constant, v is the frequency of light. I_0 is the light intensity, I_s is the photocurrent of a scintillator, S is the area of the Si photodiode detector.

Mass attenuation coefficients (μ_m) data were obtained from XCOM: Photon Cross Sections Database. Attenuation coefficients (μ) could be calculated by the following formula:

$$\mu = \mu_m \times \rho \quad \text{(S6)}$$

where ρ is density of scintillator.

Although the energy of the X-ray we used is 120 KeV, this energy is not a fixed value, and its average energy (E_{ave}) needs to be calculated. the average energy at 120 KeV X-ray can be obtained by the energy dependent for the X-ray intensity ($I(e)$) of the tungsten element (Figure S1).

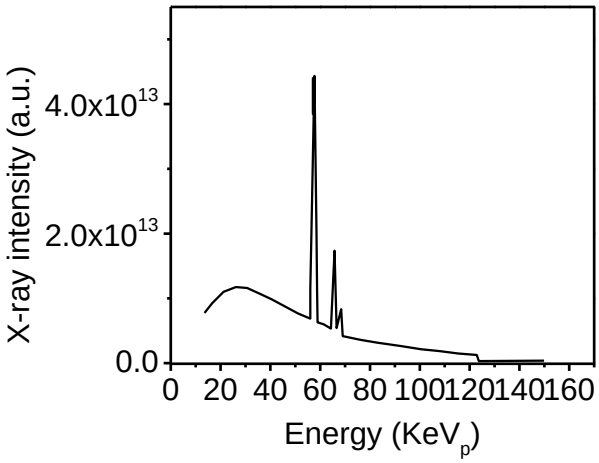

Figure S1. Characteristic peak of the tungsten at 120 KeV X-ray.

The specific calculation is to obtain the E_{ave} at 120 KeV X-ray by the following calculus formula:

$$E_{ave} = \sum_{e_0}^{e_n} \frac{e_k \int_{e_k}^{e_k+\Delta e} I(e)de}{\int_{e_0}^{e_n} I(e)de} \quad \text{(S7)}$$

where E_{ave} is the average energy of X-rays. e_0 is the lowest energy of X-ray characteristic peak of tungsten at 120 KeV, e_n is the highest energy of the X-ray characteristic peak of tungsten at 120 KeV, e_k is arbitrary energy of the X-ray characteristic peak of tungsten at 120 KeV, Δe is the amount of energy that tends to be infinitely small, $I(e)$ is X-ray intensity.

The corresponding PL decay curve of $(DABA)_2MnBr_4{\cdot}CH_3CN$ and $(DABA)_2MnBr_4{\cdot}H_2O$ gives a long average lifetime of 230 μs and 286 μs by single-exponential fitting as shown in Figure S2, respectively. Due to strong electron-phonon coupling, the long lifetimes typically originate from STEs in a distorted lattice.

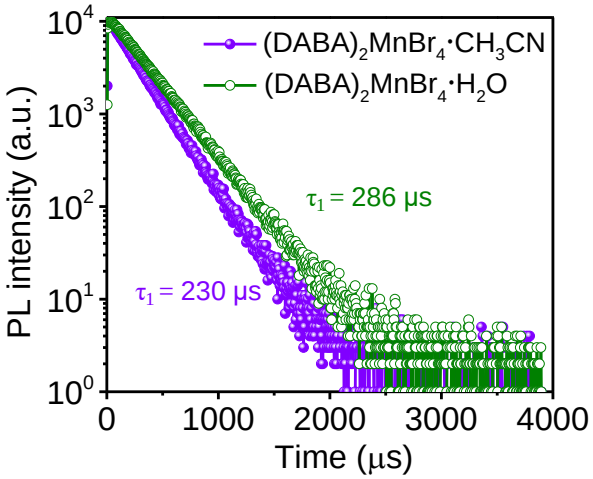

Figure S2. Time-resolved PL decay and the corresponding fitting curve of $(DABA)_2MnBr_4{\cdot}CH_3CN$ and $(DABA)_2MnBr_4{\cdot}H_2O$ at room temperature, respectively.

Figure S3 shows that two 0D lead-free perovskite structures with different ionic arrangements by co-assembling solvent molecules with perovskite ions.

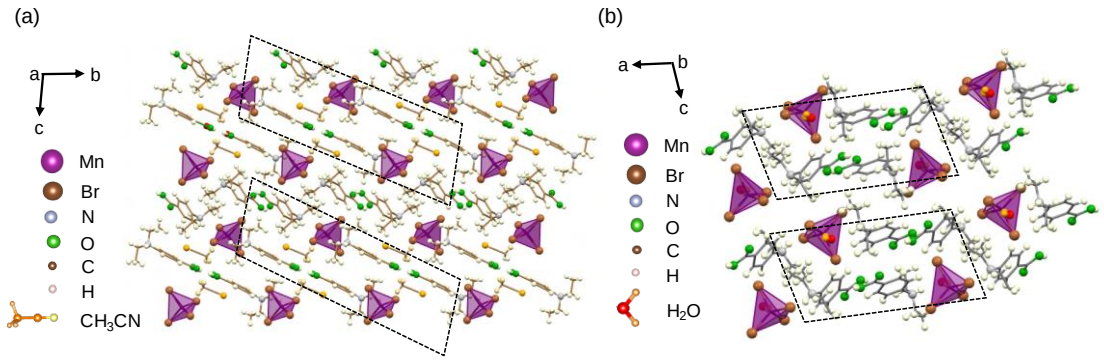

Figure S3. Crystal structure of (a) $(DABA)_2MnBr_4 \cdot CH_3CN$ and (b) $(DABA)_2MnBr_4 \cdot H_2O$, respectively.

Figure S4 shows that the thermal stability of $(DABA)_2MnBr_4 \cdot H_2O$ is higher than that of $(DABA)_2MnBr_4 \cdot CH_3CN$, which further indicates that the hydrogen bonds of $(DABA)_2MnBr_4 \cdot H_2O$ is stronger than that of $(DABA)_2MnBr_4 \cdot CH_3CN$ crystals.

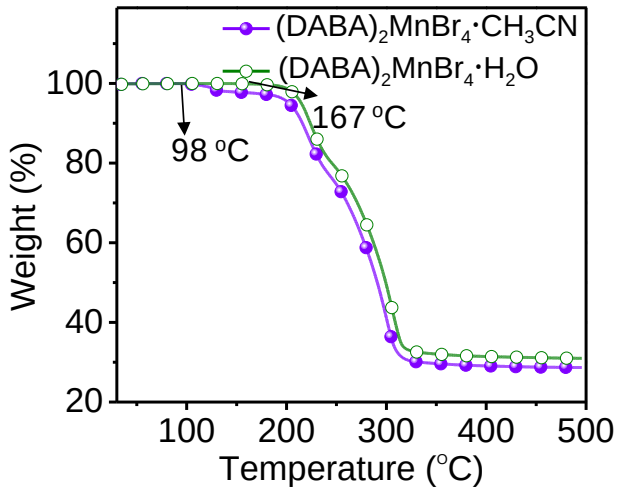

Figure S4. The TGA curves of $(DABA)_2MnBr_4 \cdot CH_3CN$ and $(DABA)_2MnBr_4 \cdot H_2O$ powder, respectively.

As shown in Figure S5, compared with the $(DABA)_2MnBr_4{\cdot}CH_3CN$ crystals, the larger barrier between H_2O molecules and organic cations makes the Mn···Mn distance longer, resulting in the more confined excitons in the $[MnBr_4]^{2-}$ tetrahedron of the $(DABA)_2MnBr_4{\cdot}H_2O$ crystals. Therefore, the photoluminescence quantum yield of $(DABA)_2MnBr_4{\cdot}H_2O$ crystals is 51%, which is 25 times higher than that of $(DABA)_2MnBr_4{\cdot}CH_3CN$ crystals.

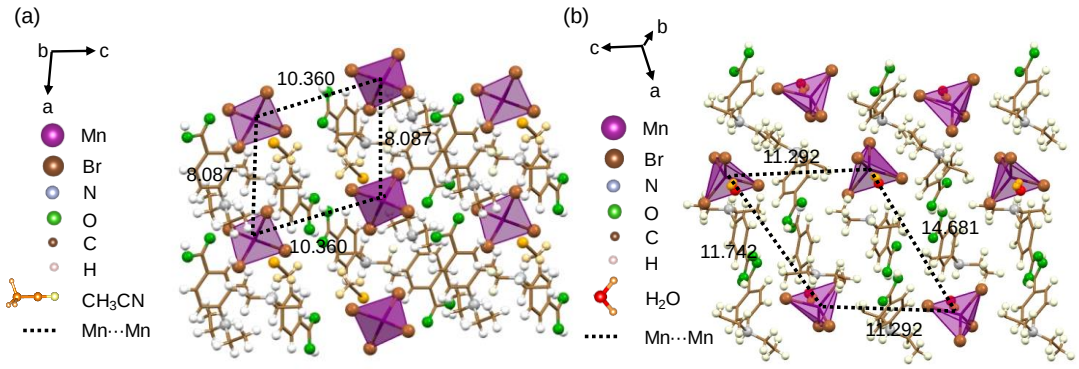

Figure S5. (a) Crystal structure of $(DABA)_2MnBr_4{\cdot}CH_3CN$, with black dashes indicating the neighboring Mn···Mn distances. (b) Crystal structure of $(DABA)_2MnBr_4{\cdot}H_2O$, with black dashes indicating the neighboring Mn···Mn distances.

As shown in Figure S6, when the monitoring emission was changed from 510 nm to 570 nm, the normalized PLE spectra of both two crystals showed similar shapes. In addition, when the excitation wavelength changes from 270nm to 390nm, the PL peak position does not change. At different wavelengths, the shape and peak position of PLE and PL spectra do not change, indicating that the green luminescence of the two crystals comes from the same excited state recombination.

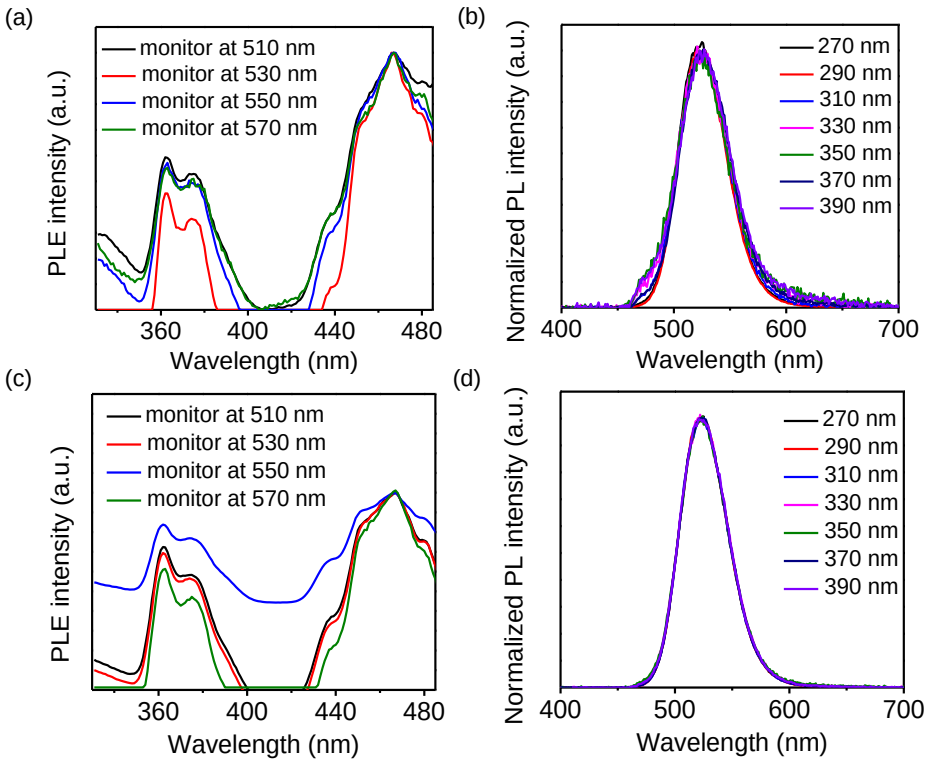

Figure S6. (a) PLE spectra and (b) PL spectra of $(DABA)_2MnBr_4 \cdot CH_3CN$ measured at different emission and excitation wavelengths, respectively. (c) PLE spectra and (d) PL spectra of $(DABA)_2MnBr_4 \cdot H_2O$ measured at different emission and excitation wavelengths, respectively.

As shown in Figure S7, the PLE spectra of both crystals are composed of three bands at 362 nm, 375 nm and 467 nm, which have electron transitions from the ground state of $[MnBr_4]^{2-}$ to excited states $[^4A_1(G), {}^4E(G)]$ (362 nm), $^4T_2(G)$ (375 nm), and $^4T_1(G)$ (467 nm), respectively. Both crystals emit green fluorescence from the $^4T_1(G) \rightarrow {}^6A_1$ radiative transition of $[MnBr_4]^{2-}$ tetrahedron (Figure S7). With the change of excitation wavelength, the shape of PL spectra does not change, which indicates that the PL emission of the two crystals comes from the same excited state radiation recombination of $[MnBr_4]^{2-}$ tetrahedron.

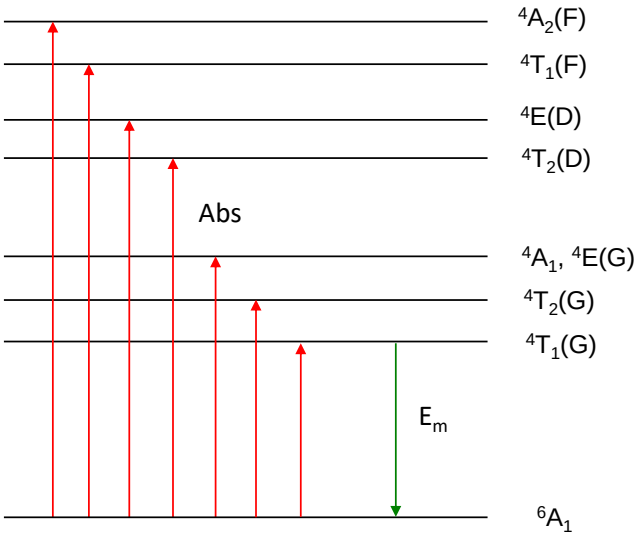

Figure S7. Schematic diagram showing the energy adsorption, migration, and emission processes of the Mn(II) complexes in a tetrahedral environment.

As shown in Figure S8, we tested the PL intensity of the two crystals with the change of excitation power density. We found a linear fitting relationship between the PL intensity and excitation power density of the two crystals, indicating that the luminescence of the two crystals is not caused by permanent defects.

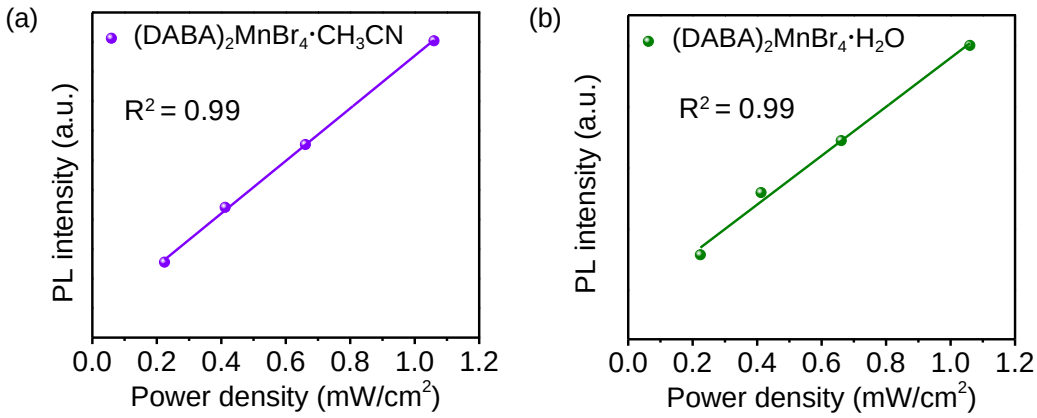

Figure S8. Power-dependent PL spectra and fitted curve of (a) $(DABA)_2MnBr_4·CH_3CN$ and (b) $(DABA)_2MnBr_4·H_2O$, respectively.

As shown in Figure S9, there is little difference in the angle of distortion of inorganic tetrahedrons between the two crystals, which indicates that the thermal quenching effect or PL efficiency difference in both of crystals mainly depends on the arrangement of organic cations.

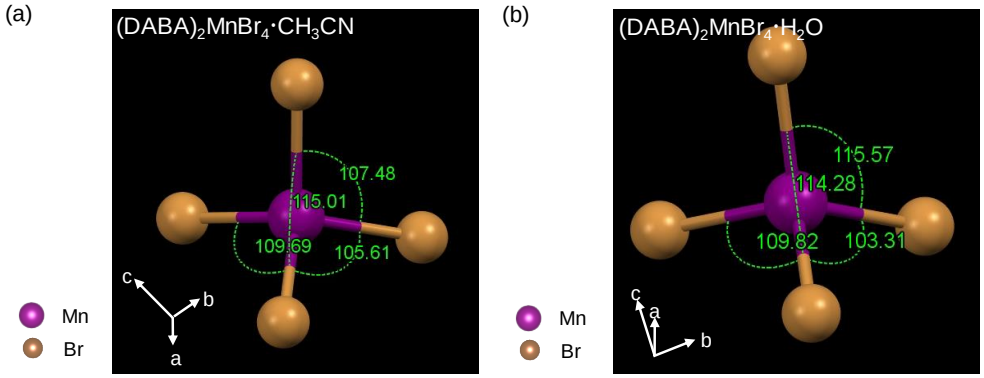

Figure S9. Structural of the $[MnBr_4]^{2-}$ tetrahedron in (a) $(DABA)_2MnBr_4{\cdot}CH_3CN$ and (b) $(DABA)_2MnBr_4{\cdot}H_2O$ crystals, respectively.

As shown in Figure S10, The $(DABA)_2MnBr_4{\cdot}H_2O$ crystals has lower formation energy than that $(DABA)_2MnBr_4{\cdot}CH_3CN$ crystals, indicating that the $(DABA)_2MnBr_4{\cdot}H_2O$ crystals is more stable than $(DABA)_2MnBr_4{\cdot}CH_3CN$ crystals.

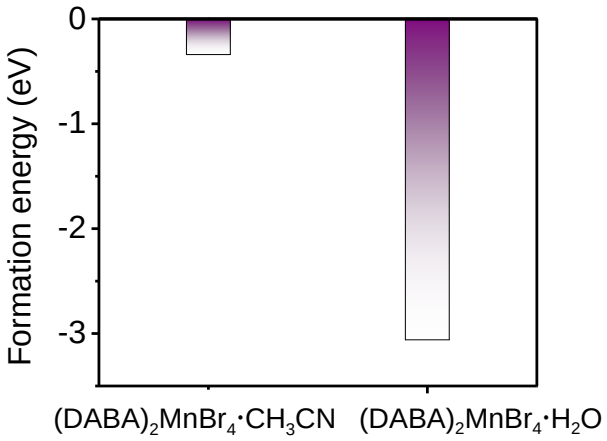

Figure S10. DFT simulation of the formation energy of $(DABA)_2MnBr_4 \cdot CH_3CN$ and $(DABA)_2MnBr_4 \cdot H_2O$ crystals, respectively.

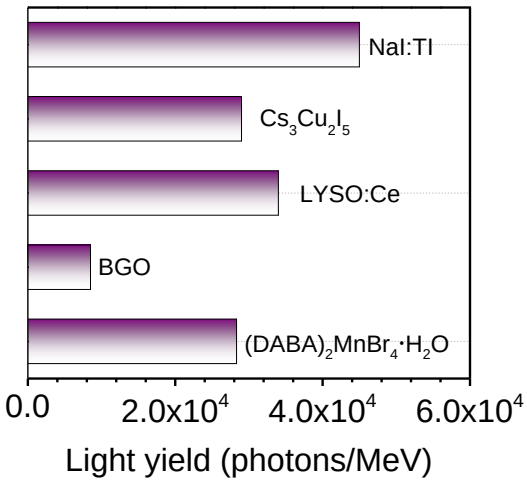

Figure S11. The light yield of scintillators.

As shown in Figure S12, we grind the $(DABA)_2MnBr_4 \cdot H_2O$ crystals into powder and make a large area scintillators with a dimension size of 2.4 cm × 3.0 cm wafer. The wafer shows high uniformity and strong emission under X-ray irradiation.

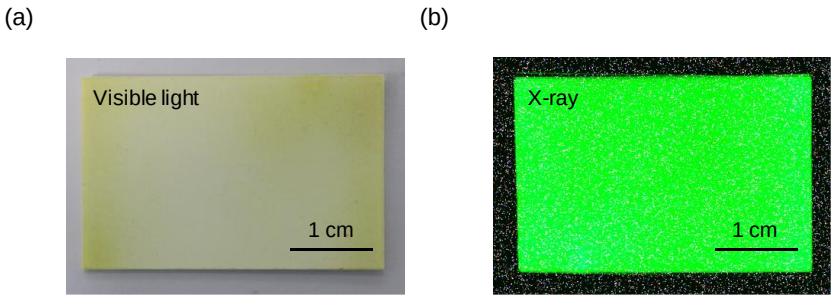

Figure S12. Photographs of large area $(DABA)_2MnBr_4 \cdot H_2O$ wafer under (a) ambient light (left) and (b) X-ray excitation (right).

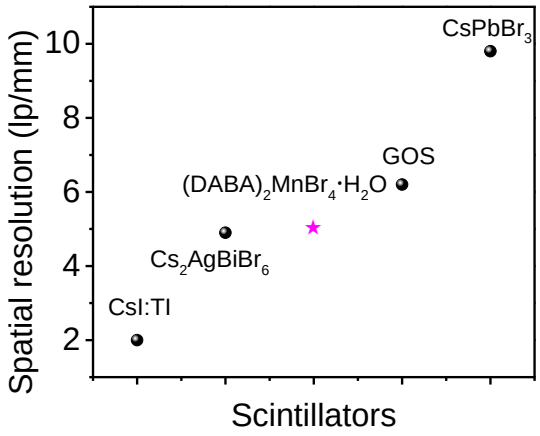

Figure S13. The spatial resolution of scintillators.

Table S1. Single crystal X-ray diffraction data of $(DABA)_2MnBr_4 \cdot CH_3CN$.

Compound	$(C_{11}H_{16}NO_2)_2MnBr_4 \cdot CH_3CN$
Empirical formula	$C_{48}H_{70}Br_8Mn_2N_6O_8$
Molecular weight	1608.26
Temperature/K	100
Crystal system	triclinic
Space group	P-1
a/Å	8.0874 (4)
b/Å	11.8756 (6)
c/Å	16.7531 (8)
α/°	94.8840 (2)
β/°	93.7269 (19)
γ/°	97.8283 (19)
Volume/$Å^3$	1583.44 (14)
Z	1
P_{calc} g/cm^3	1.687
μ/mm^{-1}	5.495
R_1, wR_2	0.0261, 0.0437
Goodness-of-fit on F^2	1.038

Table S2. Single crystal X-ray diffraction data of $(DABA)_2MnBr_4 \cdot H_2O$.

Compound	$(C_{11}H_{16}NO_2)_2MnBr_4 \cdot H_2O$
Empirical formula	$C_{22}H_{34}Br_4MnN_2O_5$
Molecular weight	781.09
Temperature/K	100
Crystal system	monoclinic
Space group	$P2_1/c$
a/Å	15.5200 (9)
b/Å	9.1212 (4)
c/Å	20.9190 (10)
α/°	90
β/°	92.088 (2)
γ/°	90
Volume/Å^3	2959.3 (3)
Z	4
P_{calc} g/cm^3	1.753
μ/mm^{-1}	5.879
R_1, wR_2	0.0222, 0.0380
Goodness-of-fit on F^2	1.069

Table S3. Summary of types of hydrogen bonds and distances in $(DABA)_2MnBr_4{\cdot}CH_3CN$ and $(DABA)_2MnBr_4{\cdot}H_2O$ crystals, respectively.

$(DABA)_2MnBr_4{\cdot}CH_3CN$		$(DABA)_2MnBr_4{\cdot}H_2O$	
Types of hydrogen bonds	Distances (Å)	Types of hydrogen bonds	Distances (Å)
(DABA) O–H···N (CH_3CN)	3.837	(H_2O) O–H···N (DABA)	3.217, 3.228
(DABA) O–H···O (DABA)	1.773, 6.731	(DABA) O–H···O (DABA)	1.767, 1.841
(DABA) N–H···Br	2.463, 4.458	(DABA) N–H···Br	2.390, 4.130
	5.382, 5.897		5.290, 5.506

Table S4. The average of the equivalent isotropic displacement parameter ($\bar{U}_{eq}$) for $(DABA)_2MnBr_4{\cdot}CH_3CN$ and $(DABA)_2MnBr_4{\cdot}H_2O$, respectively.

	$(DABA)_2MnBr_4{\cdot}CH_3CN$	$(DABA)_2MnBr_4{\cdot}H_2O$
Atom	$\bar{U}_{eq}$ (Å$^2\times10^3$)	$\bar{U}_{eq}$ (Å$^2\times10^3$)
C	23.20	17.17
O	22.28	20.04
N	26.33	20.15
Mn	17.67	15.20
Br	26.22	22.40